Volume 37 | Issues 23–24 | 2016
Included in this print edition:
Issue 23 (September 5, 2016)
**Issue 24 (September 15, 2016)**

# Journal of COMPUTATIONAL CHEMISTRY

Organic • Inorganic • Physical
Biological • Materials

www.c-chem.org

$$\begin{pmatrix} \mathbb{A} & \mathbb{B} \\ \mathbb{B} & \mathbb{A} \end{pmatrix} \begin{pmatrix} \boldsymbol{X} \\ \boldsymbol{Y} \end{pmatrix} = \Omega \begin{pmatrix} -\mathbb{1} & 0 \\ 0 & \mathbb{1} \end{pmatrix} \begin{pmatrix} \boldsymbol{X} \\ \boldsymbol{Y} \end{pmatrix}$$

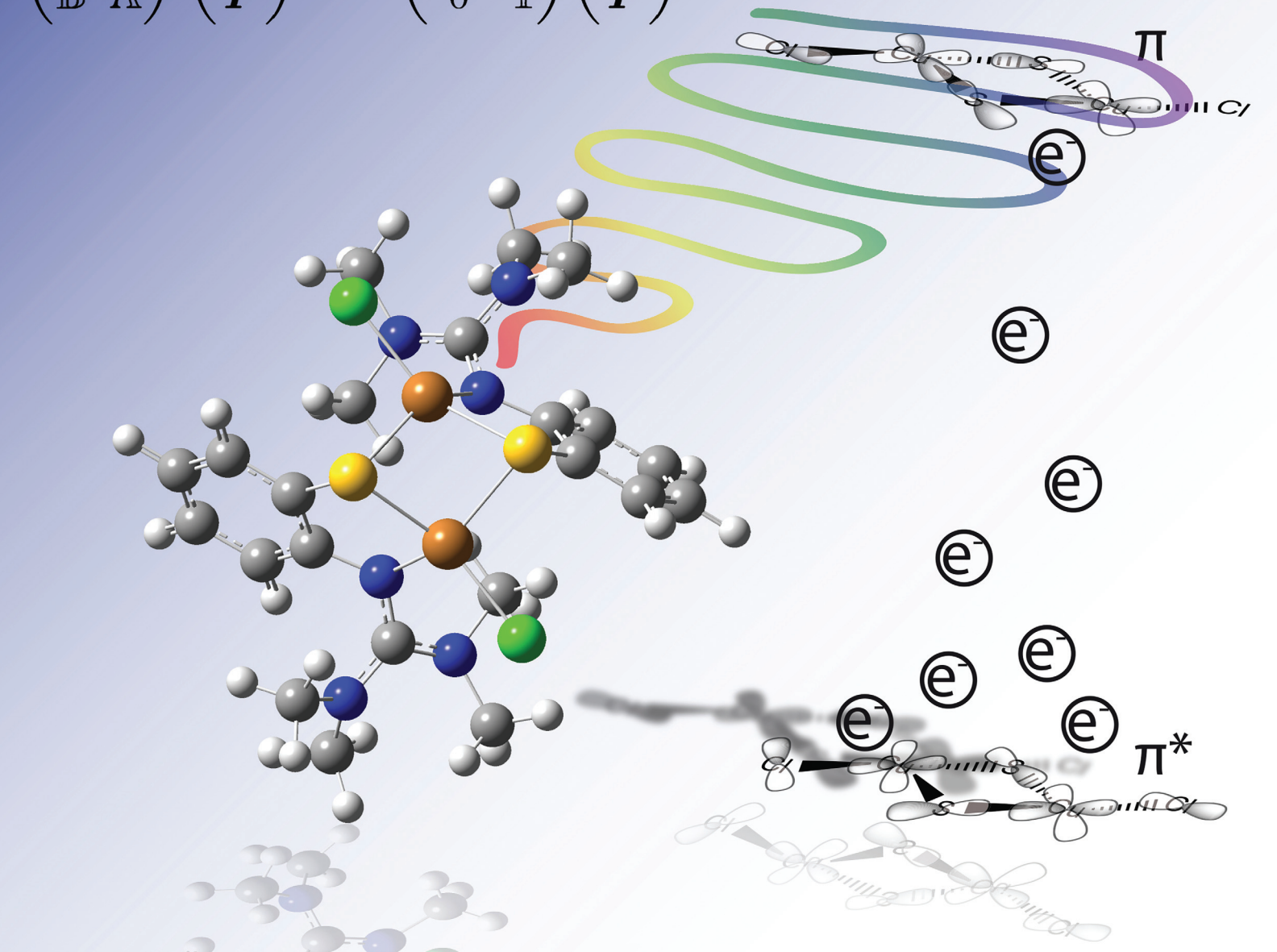




WILEY

# Optical Response of the $Cu_2S_2$ Diamond Core in $Cu^{II}_2(NGuaS)_2Cl_2$

Matthias Witte,[a] Benjamin Grimm-Lebsanft,[b] Arne Goos,[b] Stephan Binder,[b] Michael Rübhausen,[b] Martin Bernard,[c] Adam Neuba,[c] Serge Gorelsky,[d] Uwe Gerstmann,[e] Gerald Henkel,[c] Wolf Gero Schmidt,[e] and Sonja Herres-Pawlis*[a]

Density functional theory (DFT) and time-dependent DFT calculations are presented for the dicopper thiolate complex $Cu_2(NGuaS)_2Cl_2$ [NGuaS=2-(1,1,3,3-tetramethylguanidino) benzenethiolate] with a special focus on the bonding mechanism of the $Cu_2S_2Cl_2$ core and the spectroscopic response. This complex is relevant for the understanding of dicopper redox centers, for example, the $Cu_A$ center. Its UV/Vis absorption is theoretically studied and found to be similar to other structural $Cu_A$ models. The spectrum can be roughly divided in the known regions of metal d-d absorptions and metal to ligand charge transfer regions. Nevertheless the chloride ions play an important role as electron donors, with the thiolate groups as electron acceptors. The bonding mechanism is dissected by means of charge decomposition analysis which reveals the large covalency of the $Cu_2S_2$ diamond core mediated between Cu $d_z^2$ and S-S $\pi$ and $\pi^*$ orbitals forming Cu-S $\sigma$ bonds. Measured resonant Raman spectra are shown for 360- and 720-nm excitation wavelength and interpreted using the calculated vibrational eigenmodes and frequencies. The calculations help to rationalize the varying resonant behavior at different optical excitations. Especially the phenylene rings are only resonant for 720 nm. © 2016 Wiley Periodicals, Inc.

DOI: 10.1002/jcc.24439

## Introduction

Dinuclear transition metal complexes have been, and still are, of vital interest due to their biological relevance and a lot of frontier work has been done to understand the bonding mechanism in these complexes.[1–5] In particular, the $Cu_A$ site as found in cytochrome c oxidase or the nitrous oxide reductase is one of the important redox centers in biological charge transfer processes.[6–12] Hence, the dinuclear thiolate bridged copper core is a widely studied system in literature. Due to a lot of research effort its electronic as well as geometric structure is well determined by extended X-ray absorption fine structure,[9,10] electron paramagnetic resonance (EPR)[13,14] (hence $S = 1/2$), optical absorption,[15,16] low-temperature magnetic circular dichroism,[17] resonance Raman spectroscopy,[18] and X-ray crystallography.[6–8,19] It turned out that is has a dinuclear mixed valent (MV) [$Cu^{1.5+}$...$Cu^{1.5+}$] core bridged by two S(Cys) ligands. The Cu...Cu distance is quite small and ranges from 2.3 to 2.6 Å indicating a direct Cu–Cu interaction. The nature of the Cu thiolate bond is well known to be highly covalent as it is also occurring in the blue copper site, like being found in plastocyanin[20] which has been studied considerably.[21–25]

As for the biological importance, a noteworthy amount of effort has been put into synthesizing functional $Cu_A$ model complexes. Tolman et al. succeeded first, creating a MV complex (Fig. 1c).[26] A theoretical description was given by Solomon and coworkers.[29,30] The molecule has a rather large Cu–Cu distance of 2.9 Å (see Fig. 1c) excluding a direct Cu–Cu interaction. Further the complex is not reversibly reducible. A fully functional biomimetic model complex has been synthesized by Duboc and coworkers.[31] Although it also has a rather large Cu–Cu distance of 2.9 Å, it shows a, compared to natural $Cu_A$, slow but reversible reducibility.

Henkel and coworkers synthesized the thiolate bridged dinuclear copper complex $Cu_2(NGuaS)_2Cl_2$ (with NGuaS:=o-$SC_6H_4N=C(NMe_2)_2$) with a diamond core which is shown in Figure 1a.[27] The complex is formed by conversion from the corresponding Cu(I) disulfide-guanidino complex.[32,33] Guanidine ligands, being $\pi$ and $\sigma$ donors to metal bonds, play an important role in the stabilization of copper complexes.[34–41] Contrary to $Cu_A$, the diamond core of the Henkel complex is

[a] M. Witte, S. Herres-Pawlis
Lehrstuhl Für Bioanorganische Chemie, Fachgruppe Chemie, RWTH Aachen University, Landoltweg 1, Aachen 52074, Germany
E-mail: sonja.herres-pawlis@ac.rwth-aachen.de
[b] B. Grimm-Lebsanft, A. Goos, S. Binder, M. Rübhausen
Institut für Nanostruktur- und Festkörperphysik and Center for Free Electron Laser Science, University of Hamburg, Luruper Chaussee 149, 22761, Hamburg, Germany
[c] M. Bernard, A. Neuba, G. Henkel
Lehrstuhl Für Anorganische Chemie, Universität Paderborn, Warburger Str. 100, Paderborn 33098, Germany
[d] S. Gorelsky
Centre for Catalysis Research and Innovation, University of Ottawa, Ottawa, Ontario K1N 6N5, Canada
[e] U. Gerstmann, W. G. Schmidt
Lehrstuhl Für Theoretische Physik, Universität Paderborn, Warburger Str. 100, Paderborn 33098, Germany

Dedicated to Prof. Dr. Peter Klüfers on the occasion of his 65th birthday.

Contract grant sponsor: Deutsche Forschungsgemeinschaft; Contract grant number: FOR1405

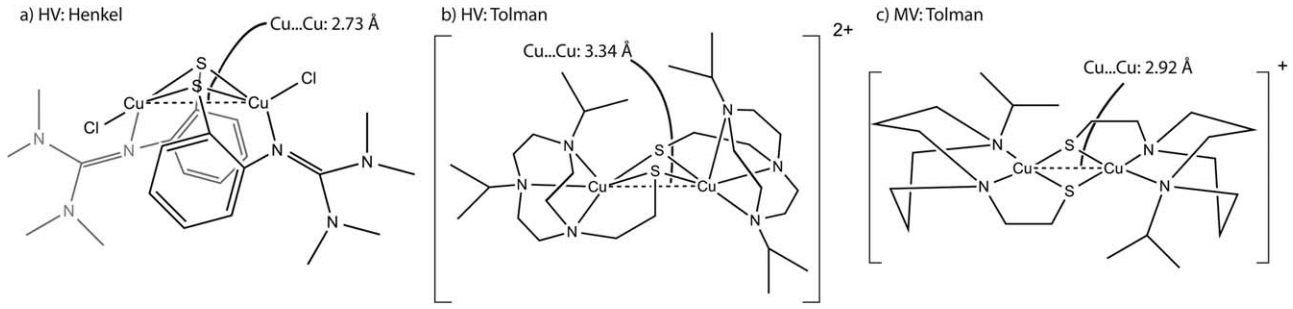


**Figure 1**. Different structural $Cu_A$ models: Two homovalent complexes by Henkel a)[27] and Tolman b)[28] and a mixed valent complex by Tolman c).[26]

not flat; hence, it shows no inversion symmetry but rather has a butterfly structure inheriting a $C_2$ symmetry (see Fig. 1a). Furthermore, the copper atoms have the oxidation state II forming a homovalent (HV) complex like the $Cu^{II}$ dinuclear complex studied by Tolman, Solomon and coworkers (see Fig. 1b).[29] But different to their complex which is reported to have a $S = 1$ ground state the complex studied here has a $S = 0$ ground state.[33] This excludes any biomimetic functionality which requires a delocalized MV core with $S = 1/2$.[42]

The theoretical description of a HV complex within the framework of density functional theory (DFT) requires the use of the broken symmetry (BS) approach as it has been introduced by Noodleman.[43–46] This procedure becomes necessary as the ground-state wave function has a multideterminantal character and cannot directly be accessed by means of DFT. Yielding the correct ground state-density the BS approach can be successfully used to describe geometrical as well as spectroscopic properties.[47–52] The electronic configuration of the ground state has been elaborately discussed in Ref. [33] and the implications of the BS ansatz with respect to the description of the exchange correlation (xc) functional are studied. It is found that the inclusion of the kinetic energy density by the meta GGA xc functional TPSSh[53–55] is crucial to describe the proper geometry of the molecule. In this study, we pursue the work and analyze the bonding mechanisms of the $Cu_2S_2$ core. Furthermore, we extend it to calculations of the optical UV/Vis spectra in the frame of time-dependent density functional theory (TD-DFT) and compare it with the experiment. Additionally resonant Raman measurements are shown and the measured spectra are assigned to the calculated normal modes.

## Methods

### Computational methods

The DFT as well as the TD-DFT calculations presented here are done with the Gaussian09 software package, revision D.01.[56] The TPSSh exchange and correlation functional[53–55] has been found to yield a reliable molecular structure.[29] The inclusion of dispersion interaction is particularly vital for the determination of the correct structure in gas phase.[33] The dispersion forces are modeled here using the post-scf method by Grimme with the Becke and Johnson damping.[57,58] The correlation consistent split-valence double zeta (cc-pVDZ) basis[59–61] is shown to be sufficient. Hence, the presented results are solely done within these approximations if not stated otherwise. The minimum energy state is reached with a broken-symmetry approach as described in the introduction. The optical absorption is calculated with the Casida equation originating from the linear response theory in the TD-DFT framework.[62] The charge decomposition analysis (CDA) is done with the AOMix program package[63] in combination with Gaussian09 preparing the fragmented calculations. In detail, one is fragmenting the molecule into different parts and assigning each fragment a chemical meaningful charge and multiplicity. Each individual fragment is then self-consistently (sc) solved. These resulting wave functions with their MOs then serve as a new basis to form the full complex and are used for the CDA. Furthermore, they can be used as starting guesses for the combined whole complex in a non-sc (nsc) calculation. The nsc energies can be compared for different charges and multiplicities. This is used to gain insight in the bonding mechanisms and the related charge transfer.

### Raman experiments

For the resonant Raman experiment, a McPherson Ultimate Triple 3 (UT3) Spectrometer[64] was used in conjunction with a pulsed Ti:Sapphire, Tsunami model HP ps 10 W P (Spectra Physics Lasers, CA) which was pumped with a green Millennia Pro Xs 10sJS diode laser (Spectra Physics Lasers, CA). The fundamental laser line was used for the 721.1-nm measurements, the frequency doubled $2\omega$, with a FHG, model GWU2 23-PS (Spectra Physics Lasers, CA) was used for the 361.2 nm measurements. The used laser power in front of the entrance optics was, depending on the wavelength, between 4.4 and 24.5 mW. The experiments were conducted in a cleanroom with constant temperature (22.0°C ± 0.5°C) and humidity (40 ± 3%). All experiments were done at room temperature. To get the pulse width of the laser, a small part of the Tsunami fundamental was mirrored out using a glass plate and the reflex was then coupled into an autocorrelator (APE GmbH, Berlin, Germany). For *x*-axis calibration and optimization of the optical pathway, a silicon substrate was adjusted in the laser focus of the UT3 entrance optics. The beam path was adjusted so that a maximum silicon peak intensity was found. As the wavenumber of the silicon peak is known, this position was used to calibrate the *x*-axis of the spectra.

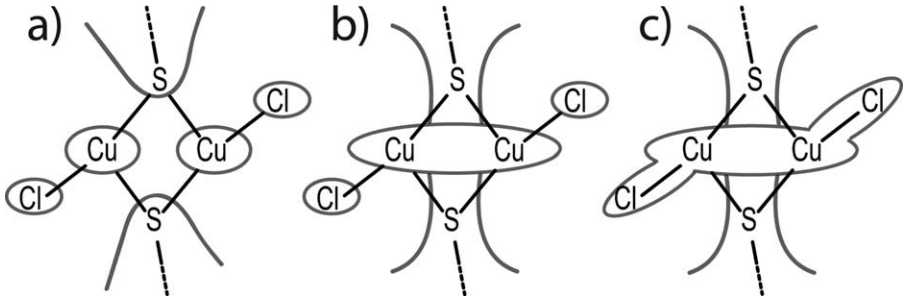


**Figure 2**. The three different used fragmentation schemes for the complex.

For the measurements, a Suprasil glass cuvette (Hellma Analytics, Müllheim, Germany) was filled with 3 mL solution of the complex solved in DCM or MeCN with a concentration of 5 mmol/L. The solution was continuously stirred with a magnetic stirring system. The cuvette position inside the UT3 entrance optics was adjusted with a micrometer screw so that at first the laser focus was on the outside glass reflex of the cuvette then on the inside glass reflex and subsequently 80 μm inside the solution.

Before each measurement the laser power was measured using a LM-1 power meter from Coherent. Afterwards the camera background was substracted and the spectra were white light corrected using an Ulbricht Kugelsystem (Deutscher Kalibrierdienst, Gigahertz-Optik, Puchheim, Germany). All measurements were normalized to an integration time of 1 s and a laser power of 1 mW. All measurements were constant in time and the median of at least three measurements is shown.

For comparison with the absorption profiles, the measured intensities were corrected for wavelength dependent absorption. The wavelength dependent absorption was measured using UV/Vis spectroscopy and the measured intensities were corrected using a correction factor

$$A_{\text{norm}} = \frac{I_0 - I_t}{I_0} = e^{-2.3\varepsilon cd}$$

where $I_0$ is the initial intensity, $I_t$ the transmitted intensity, $\varepsilon$ the molar absorption coefficient, $c$ the concentration, and $d$ the path length of the laser inside the solution.

## Results and Discussion

The HOMO-LUMO (H,L) characteristic of the ground state configuration is already known. Both are equally given by about 30% Cu as well as S contributions.[33] Nevertheless, the details of the chemical bonding of the complex and its relation to the $Cu_A$ specific functionality are still unknown. Hence, the molecular orbitals will be characterized and discussed in comparison with $Cu_A$-like systems known from the literature. Having these results in mind, we will unravel the spectroscopic properties, for example, the UV/Vis absorption and present resonance Raman spectra along with a justification of the enhancement by comparing spectra with different excitation energies with theoretically obtained modes.

### CDA analysis

In Ref. [33], the oxidation state of the complex has been discussed at length. In comparison with copper chloride salts, it has been found that the occupation of the *d*-electrons rather correspond to a $d^9$-configuration. Nevertheless, it is of interest how the different ligands contribute to the final charge distribution. Hence, we perform a CDA by fragmenting the molecule differently providing different starting charges. Only chemical meaningful guesses that end up in the correct BS state are considered. Thus, it is necessary that the guess already inherits a symmetry break in the spin distribution. This can be either achieved by the two Cu ions having the assumed $d^9$-configuration or the two NGuaS ligands having thiyl radicals which would imply that they are neutral and the Cu ions have a $d^{10}$ configuration. Several fragmentation schemes are possible: A first guess might be to separate the two Cu ions to induce a spin flip (see Fig. 2a). The next possible guess is to couple the two Cu into one fragment (Fig. 2b) to allow for a direct exchange coupling along with the two coupled NGuaS ligands in one fragment. A third guess is built up on this by incorporating the two Cl ions (Fig. 2c) into the Cu. . .Cu fragment.

One would expect that the guess wave function having the lowest energy would correspond to the correct oxidation state as well. Nevertheless, irrespective of the fragmentation, the Cu(I) guesses being bridged by neutral but radical guanidinethiyl fragments are always more stable in energy as shown for fragmentation scheme c) shown in Figure 3.

One has to keep in mind that only starting guesses with the same fragmentation must be compared as the already existing bonds in a fragment alter the total energy and only cancel out, if they are kept constant. The energy gain between the different fragmentation types is originating in the number of formed bonds within the fragment and is hence not relevant. The different other guesses along with their energy are shown in the Supporting Information in Table S1. The reason for the Cu(I) guesses being energetically more stable than their Cu(II) counterparts originates from the low net charge (NBO: 0.49 $e^-$) within the complex.[33] This low net charge is due to the high covalency of the Cu—S bond.[27] The required charge relocation from the Cu(II) guesses reduces the guessing energy making them less favorable. Another way to judge MO interactions and especially bonding interactions is analyzing the overlap population (*OP*) formed by the overlap *S* of the localized

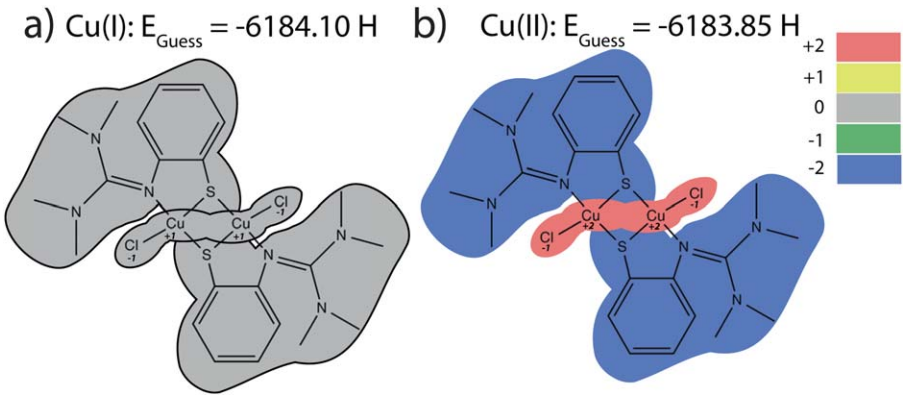


**Figure 3**. Possible two fragment scheme for a) Cu(I) and b) Cu(II) configurations with resulting guessing energies. [Color figure can be viewed in the online issue, which is available at wileyonlinelibrary.com.]

basis functions $\varphi$ and the wave function coefficients $c_{ai}$ of the *i*th eigenstate.

$$S_{ab} = < \varphi_a | \varphi_b >$$

$$OP_i = \sum_a \sum_b 2 c_{ai} c_{bi} S_{ab}$$

As one cannot distinguish between bonding and antibonding character in the *S* matrix one uses the *OP* matrix: A positive sign means a bonding interaction, a negative sign antibonding. A vanishing *OP* denotes a non-bonding interaction.[65–67] Looking at the total *S* and the total *OP* (summed up over all occupied states) for the diamond core one can rule out any S–S interaction, as both values are one magnitude smaller than for the Cu Cu interaction, see Table 1.

Therefore, the BS interaction is transmitted via the copper atoms indicating a $d^9$ configuration. Hence, one can conclude that the formal concept of oxidation states might help in finding interacting sites but they do not necessarily correspond to real charge distributions due to complicated many body interactions. A detailed discussion of this issue can be found for example in Refs. [68,69]. Nonetheless, based on this one can build up a fragmentation scheme to analyze the diamond core bonding according to Figure 3b, where the two CuCl are antiferromagnetically coupled and interact with two symmetric NGuaS ligands. Within this scheme, one can identify how the different orbitals are composed by the fragmental orbitals, as shown in Figure 4 for the frontier orbitals. Already for the these MOs one sees that the composition is often by far not simple and does not enlighten anybody in terms of bonding between the $(CuCl)_2$ and $(NGuaS)_2$ fragments as not every fragment orbital (FO) of an MO is interacting with every other FO of the other fragment in a bonding way, as we will discuss in the next section in detail.

**Table 1.** Absolute value of the total overlap *TS* and total overlap population TOP between the diamond core atoms and the adjacent ligands in units of e.

| | $\|TS\|$ | TOP |
|---|---|---|
| Cu Cl | 18.0 | 0.58 |
| Cu S | 22.5 | 0.44 |
| Cu S | 22.1 | 0.29 |
| Cu Cu | 27.7 | −0.61 |
| S S | 2.1 | −0.06 |
| Cu N | 2.07 | 0.34 |

### Bonding analysis

It is clear, that the bonding orbitals of the diamond core are composed of Cu *d*- and S *p*-orbitals but as the copper and chloride couple to a BS state it is interesting how they interact with the NGuaS fragment bonding the diamond core. In literature, the bonding motif of the $Cu_A$ diamond core is explained via a smaller model core incorporating the $Cu_2S_2$ unit and two ammonia molecules, each bonding to the Cu ions. The model inherits a perfectly symmetric (flat) $D_{2h}$ configuration.[17] Along with further calculations this model core is also used to explain the $Cu_A$ EPR signal.[70] The diamond core bonding is dominantly assigned to highly symmetric interaction incorporating the Cu *d*- and S *p*-orbitals (see Fig. 5a). Due to the short Cu. . .Cu distance, the Cu ions are directly bonded by a $\sigma$-bond and a Cu-Cu-$\pi$ bond including S *p*-contributions.

Furthermore, the $Cu_2S_2$ core is stabilized by two MOs forming completely Cu *d*-S *p*-$\sigma$ bonding interaction over the whole diamond core, compare Figure 5a, $\pi_g$ and $\sigma_u$. Rather than being flat, the here studied model has a butterfly structured diamond core and the molecule inherits only a $C_2$ symmetry (compare Fig. 1a) which is even broken by the lacking spin symmetry, hence we cannot expect to find such nicely oriented bonding MOs like in the $Cu_A$ model. In Figure 6, we show four different model cores. It is well known that the coordination environment of the metal atoms is crucial for the hybridization of the metals' *d* orbitals and hence for their bonding behavior.[1,2] Therefore, one cannot expect to find any good representation for the set of MOs in the model cores (a) and (b).

Nevertheless, it is noteworthy that it is not possible to stabilize a BS configuration with the model core (a) (see Fig. 6). If the chloride is missing, the $\alpha$-, $\beta$-wave function, respectively, cannot delocalize as much at one of the chloride atoms (see H-17 to H-29, Fig. 4). Consequently both spin orbitals coincide spatially at the Cu ions, forming enough overlap to stabilize a

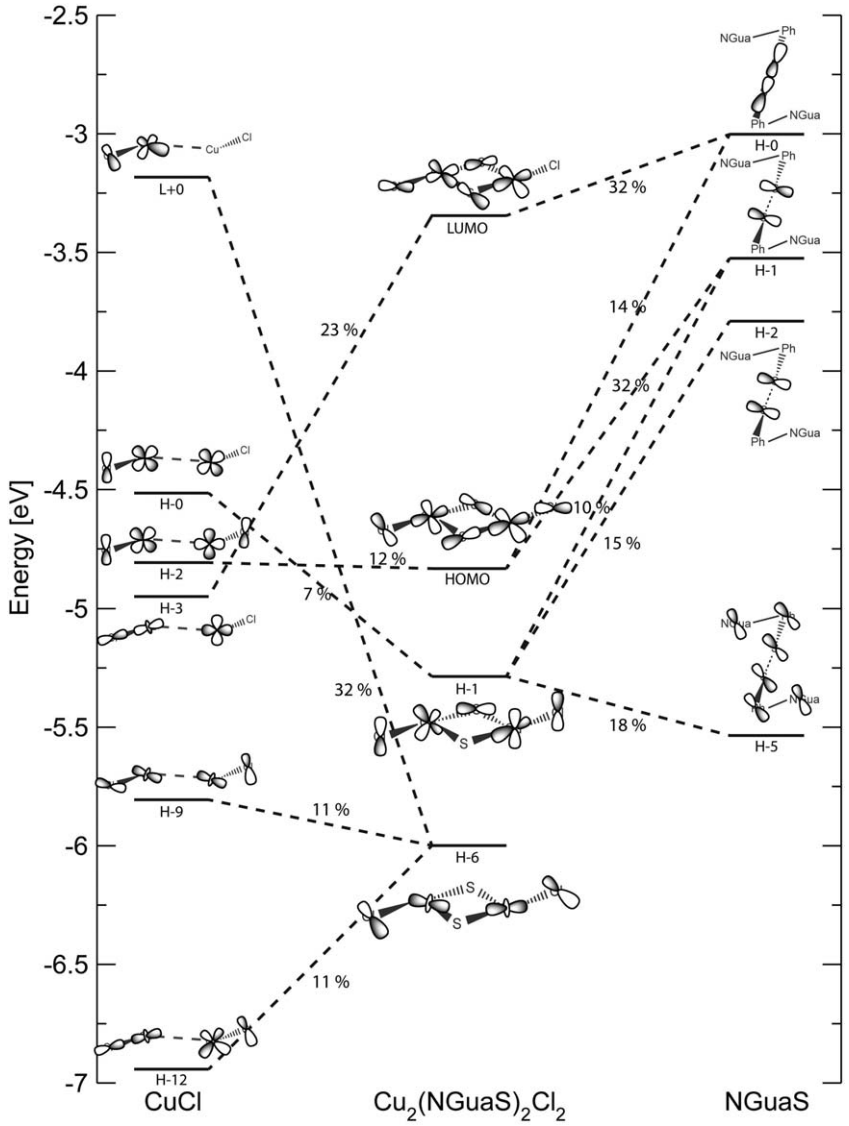


**Figure 4**. Molecular interaction picture of the $\alpha$-frontier orbitals for a Cu(II) fragmentation. Only contributions over 10% are shown, except there are only lesser ones which still significantly contribute to the MO.

closed shell singlet solution. The model core (c) has the right coordination of the metal atoms but is still not suitable for an MO representative: Due to the missing NGua ligand, most S *p* orbitals are oriented along the Cu–Cu axes and the Cu S bond is overestimated. If thiomethylate is used instead as in the already quite large core (d) the orbitals can be, most of the time, correlated one to one to the full complex. In all other cases the MOs are, as expected, composed by a different superposition of the atomic orbital (AOs). This is in accordance with the work of Takano et al. who have also shown that small model cores are not sufficient in finding the correct ground state wave function.[71]

For analyzing the bonding mechanism between the $(CuCl)_2$ fragment and the NGuaS ligand in the diamond core, we begin by identifying the bonding orbitals via the *OP*-matrix, see S2. As we already have the decomposition in terms of the FOs, we can analyze the *S*- and *OP*-matrix between the MO composing FOs and can give a detailed picture of which FOs contribute to the bonding mechanism in each diamond core stabilizing MO for the full complex, only by means of different DFT calculations! For the sake of readability and length of the paper, the bonding decomposition of the diamond bonding MOs can be found in Table S3 along with pictures of the Kohn-Sham orbitals in S4. For a better view, only one spin channel is shown, the other one is rotated by $\pi$ and inverted in its phase due to the broken-symmetry character of the ground state. Here, we discuss a typical bonding MO, the H-23 as shown in Figure 7. For this MO, the $(CuCl)_2$ fragment has an overlap population of 0.05 with the $(NGuaS)_2$ fragment, and one observes that on the one side each S *p*-lobe forms a $\sigma$ bond with one opposing Cu *d*-lobe. On the other end, one lobe of a Cu $d_z^2$-orbitals bonds with the other end of a S *p*-orbital, forming a $\sigma$ bond. This bonding mechanism is composed of two sets of two FOs interacting with each other, see Figure 7. The H-4 (CuCl fragment), having a Cu $d_z^2$ as well as a $d_{xy}$ orbital interacts with the H-9 of the NGuaS fragment which

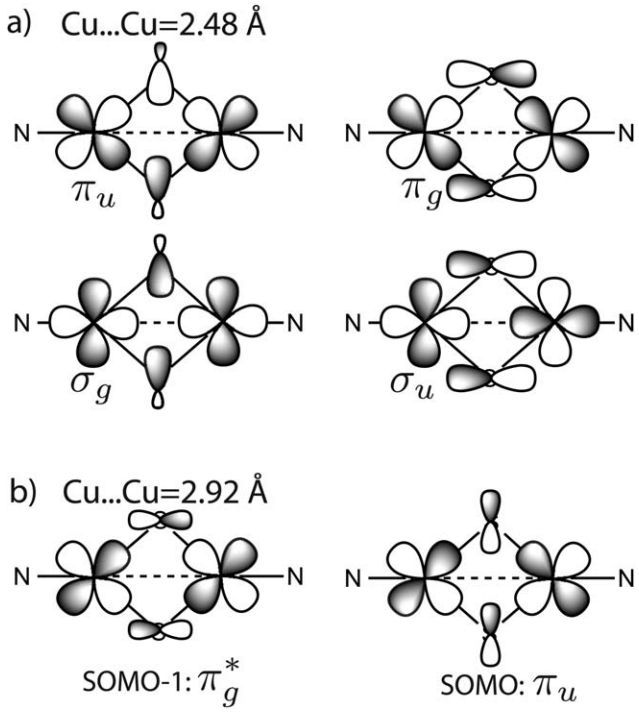


**Figure 5**. Theoretically determined bonding MOs of the $Cu_2S_2$ motif for a short Cu...Cu distance as provided by Farrar et al.[17] a) and the two highest occupied MOs in the MV and HV complex discussed by Gamelin et al.[29] b) as shown in Figures 1b and 1c.

is a formed by two opposing *p*-orbitals at the S forming a $\pi$ bond with the phenyl ring. A further bonding interaction is induced between two opposing Cu $d_{xz}$-orbitals (FO: H-7, $\delta$*) and a $\pi$* S-S antibonding FO (H-1).

In general, one can identify the diamond core stabilizing orbitals as rather low lying MOs, between H-15 and H-30, which is due to the rather small energy splitting of low lying, anti- and nonbonding mainly NGuaS dominated MOs. Furthermore, it is noteworthy that not the main contributing FOs of an MO contribute to the bonding mechanism but rather the small FO contributions, often below ten percent, form the bonding interaction. Overall one can identify four FOs of each fragment, respectively, shown in Figure 8, which contribute in sum to 68% to all bonds.

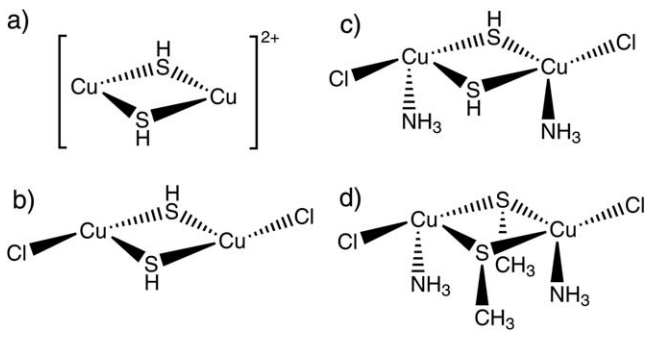


**Figure 6**. Four different model cores for analyzing the bonding MOs of the full complex.

Hence, mostly Cu $d_z^2$-FO (H-4,H-8,H-9) transmit the bonding interaction from the Cu side along with the H-7 which are two opposing antibonding $d_{xz}$-orbitals forming a $\delta$* interaction. The H-4 FO illustrates how the broken-symmetry nature of the complex complicates the situation as it combines a $d_z^2$ and $d_{xy}$ on each copper respectively. On the NGuaS fragment the bonding FOs are either a S-S $\pi$ bonding or $\pi$* antibonding interaction respectively (H-1/H-2) mediating the bonding or a $\sigma$ or $\pi$ bond between the phenyl ring and the S which then bonds to one Cu site (H-6/H-9). Hence, for the full complex, the main bonding mechanism of the diamond core can be simplified to only four FOs on each fragment!

Compared to the model core discussed earlier by Farrar et al.[17] (Fig. 5a), where Cu $d_z^2$-orbitals are only contributing to non-bonding MOs, here they actually play an important role: We find that the Cu $d_z^2$ not only mix into most orbitals, it is then forming $\sigma$ bonds with the S *p*-orbitals stabilizing the diamond core. Analogous to the $Cu_A$ model (Fig. 5a), $\sigma$ bonds are formed between the Cu *d*- and S *p*-orbitals but they are often going along with a $\sigma$ bonding with the Cl *p* orbitals (c.f., H-16, −22, −23, −29). The Cu-Cl bond is also transferred by $\pi$ binding orbitals whereas the Cu $d_z^2$ has to bend quite much (H-17/18). Especially, the H-17 shows how the complicated asymmetry of the complex affects the MOs: The Cl *p* forms a $\pi$ bond with the torus and the lobe of the Cu $d_z^2$ AO. But the same lobe is also involved in a $\sigma$ bond with the guanidine. The opposing Cu $d_z^2$ lobe is forming a further $\sigma$ bond with the S *p* orbital which is directly ongoing to the phenyl ring. Although the Cu...Cu distance is larger than 2.5 Å one can still find a weak $\sigma$ Cu-Cu bonding orbital as shown in Figure 5a at the H-6 (Fig. 4). But it is rather transmitted via two Cu $d_z^2$-orbitals which are contributed from the FO H-9 with an *OP* of 0.03 between the Cu ions, see Figure 8. Nevertheless this is just one orbital and the total Cu–Cu interaction is strongly antibonding as can be seen from the *TOP*, Table 1.

Conversely, the distance is too large for the HOMO to form a $Cu_A$-like $\sigma_u$* MO. This orbital is in the MV case the EPR active singly occupied molecular orbital (SOMO).[17,29,70,72,73] Tolman and Solomon and coworkers analyzed a MV as well as a HV complex with a longer Cu...Cu distance of 2.92 and 3.34 Å, respectively (see Fig. 1) and found for the MV species that the SOMO-1 and SOMO have $\pi$* and $\pi$ character (Fig. 5b). This characteristic is kept for the HV case, where the SOMO becomes the LUMO and the SOMO-1 is the doubly occupied HOMO.[29]

The HV complex by Henkel shows the same characteristic orbitals as shown in Figure 9. The HOMO and LUMO can be seen as a $\pi$* and $\pi$ interaction of the Cu ions, although they do not bond directly but rather interact via the bridging ligands. The sulfur orbitals are just as in the Tolman complex more or less orthogonal between the HOMO and LUMO. After all, the distorted symmetry as well as the BS character makes a bonding analysis of the diamond core not trivial but with a carefully performed CDA one can narrow it down to primarily Cu $d_z^2$-orbitals interacting with a S...S $\pi$ bridge, which is broken up to form Cu-S $\sigma$ bonds, stabilizing the diamond core.

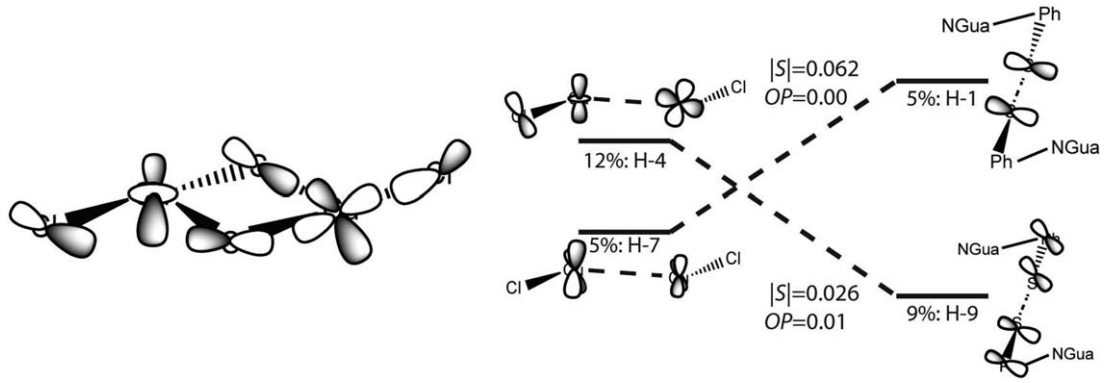


**Figure 7.** Decomposition of the H-23 (left side) in only bonding contributing FOs (right) for one spin channel. The percentage value indicates how much the bonding FO contributes to the whole MO among other nonbonding FOs (not shown). Dashed lines indicate bonding interaction between the FOs.

### UV/vis spectroscopy

The experimental UV/Vis spectrum has been examined (solved in dichloromethane) by Neuba et al. and they found "two S → $Cu^{II}$ ligand-to-metal charge transfers transitions" at 590 and 708 nm (2.10 and 1.75 eV), respectively, "and a weaker S → $Cu^{II}$ band at 419 nm" (2.96 eV) (Table 2).[27] To understand these transitions, we calculate the absorption spectrum by solving the Casida equation within the TD-DFT approach. Thereby up to 150 excitations are taken into account. The results are shown in Figure 10. Looking at the gas-phase spectra one sees that the measured double peak structure around 260 nm (4.75 eV) is not reproduced. The peak around 419 nm (2.96 eV) is redshifted toward 466 nm (2.66 eV), whereas the peak at 708 nm (1.75 eV) is blueshifted toward 666 nm (1.86 eV).

The situation looks different if the solvent is included via a Polarizable Continuum Model.[74–76] An additional peak rises at 238 nm (5.2 eV) forming the expected double peak. Another peak comes up at 406 nm (3.05 eV, labeled b)) close to the experimental peak. The former blueshifted peak is going to smaller energies (751 nm/1.65 eV, peak (a)) getting 12 nm (0.1 eV) closer to the experimental peak. To understand these differences, we take a look at the calculated term schemes for the two situations (Fig. 11). The redshift at 751 nm (1.65 eV) can be explained due to the smaller shifts of the occupied levels below the HOMO compared to the LUMO. The additional peaks at 406 nm (3.05 eV) and 238 nm (5.2 eV) can be reasoned by an energetic level splitting of the electronic states around −5.5 eV and 1 eV respectively. A one to one match with the experimental peaks and major theoretical excitations is given in Table 2.

To understand the excitations individually, we perform a Natural Transition Orbital (NTO) analysis where Highest

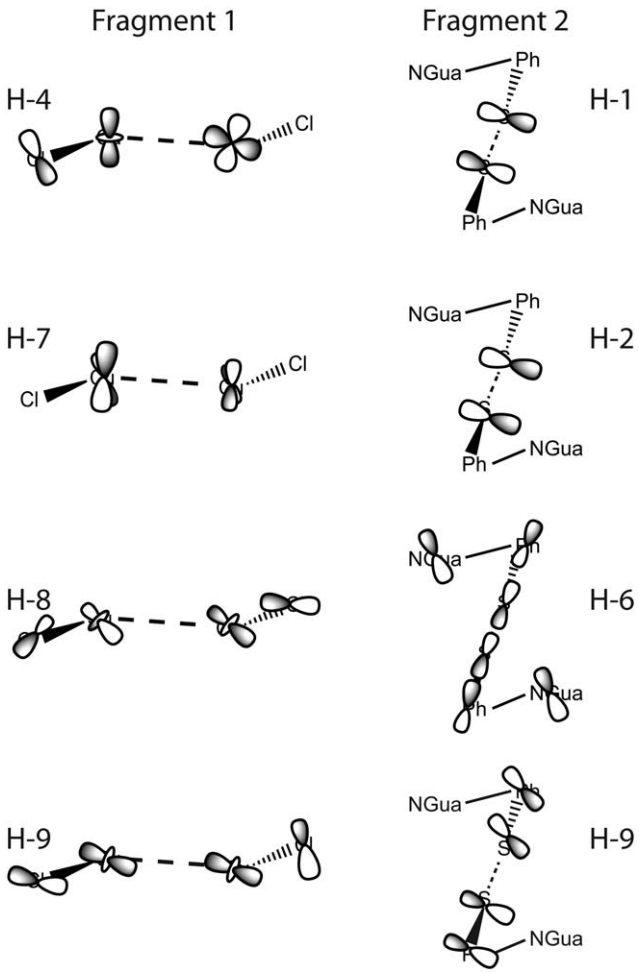


**Figure 8.** Schematic representation of the α-FOs which contribute to 68% to the diamond core bonding in total.

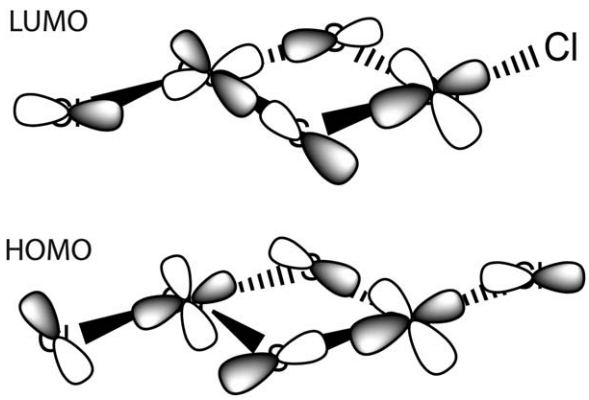


**Figure 9.** Schematic illustration of the π LUMO and π* HOMO. For clarity, only one spin channel is shown.

**Table 2.** Experimental excitations,[27] matched theoretical excitations with their interpretation, and assigned peaks of the HV Tolman complex.[29]

| Exp. | Theo. | HV Tol. | Major excitations |
|---|---|---|---|
| 708 (1.75) | 760 (1.63) | 675 (1.83) | Ngua, Cu → S, Cu |
| 590 (2.10) | 560 (2.21) | 599 (2.07) | Cl, Cu → Cu, S |
| | 477 (2.60) | 448 (2.76) | Cl, Cu → Cu, S |
| 419 (2.96) | 399 (3.11) | 410 (3.03) | Cl, Cu → Cu, S |
| | 332 (3,73) | 338 (3,68) | Ngua, Cu → Cu, S |
| 275 (4.51) | 269 (4.60) | | Cl, S, Cu → Ngua |
| 243 (5.10) | 236 (5.25) | | Cl, Ngua, Cu → ph |

First number is in nm, the value in parentheses in eV.

Occupied Transition Orbital (HONTO) and Lowest Unoccupied Transition Orbital (LUNTO) are visualized and compared by calculating the transition density difference.[77] A detailed analysis shows that the optical transition can be divided into two basic sections: Down to 340 nm (3.6 eV) all transitions spread into the LUMO, hence the $Cu_2S_2$ diamond core (*d* and *p* orbitals respectively). Going to smaller wavelengths, the absorption is in higher energy levels being mainly composed of phenyl-$\pi$ orbitals. For a better visualization, the HONTO LUNTO pairs are shown for one characteristic peak in the small, mid, and long wavelength region in Figure 12, all associated HONTOS and LUNTOS are shown in the Supporting Information along with the transition density, Table S5. One finds for the larger wavelength side of the spectrum that it is composed of transitions from the ligands into the $Cu_2S_2$ diamond core and within the Cu *d* orbitals. In the lower end of the spectrum, this is reversed and one observes transitions from the Cu *d* orbitals into the phenyl ligands, compare Figure 12 c).

Hence, the characterization in Ref. [27] is qualitatively mainly correct. However, it has to be noted that the above excitations occur also within the Cu *d* orbitals, and that chloride plays an important role as electron donor for the peak at 419 nm. Compared to the HV Tolman model in Ref. 29 (see Fig. 1b), the $Cu_A$ typical low lying $\pi^* \rightarrow \pi$ (HOMO–LUMO, see Fig. 5b) transition cannot be observed as well. The excitations for the HV species are not given explicitly, so they have to be extracted graphically and are listed in Table 2. A comparison shows that each peak can be assigned to an excitation in Figure 10 and that they are quite close with respect to their excitation energy. Only down to 300 nm (4.1 eV) whereas a combination of absorption and MCD identifies nine excitations in this region for the Tolman complex.[29] Nevertheless, the calculations yield additional excitations which were resolved experimentally, see Figure 10 and Table 2. The calculated signals at 477 (2.6) and 332 nm (3.73 eV) can be related to the signals 448 (1.76) and 338 nm (3.68 eV), respectively. Despite the fact that both complexes have a different ground state wave function ($S = 1$ and $S = 0$, respectively) and different ligands (the equatorial N being substituted by a Cl in the Henkel complex, see Fig. 1) both spectra show roughly the same characteristics. This leads to the conclusion that the Cu and S atoms are not only dominant for the MO shape but also for their relative energetic position to each other and therefore the excitation energies.

### Raman vibrations

To investigate further on the diamond core interaction, we calculate the vibrational eigenmodes along with the Raman intensities of the complex and identify the Cu-S related modes. Raman spectroscopy is here an ideal tool as it allows the selective excitation into an absorption band.[78] While the BS approach yields in principle a correct description of the electronic ground-state density, the molecular structure calculated

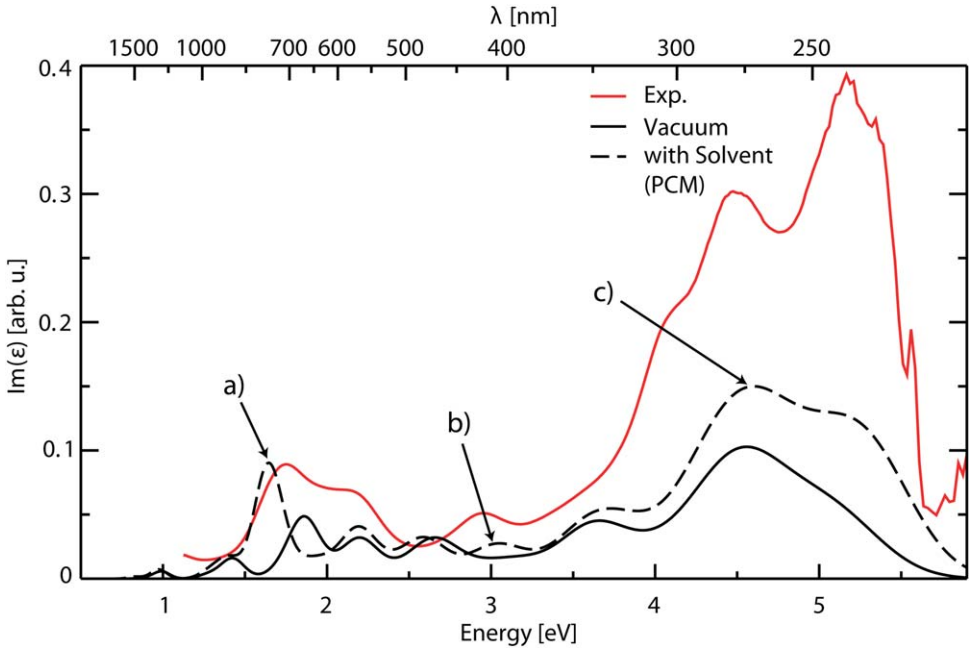


**Figure 10.** Experimental and calculated (TPSSh + D3BJ/cc-pVDZ) optical absorption with and without consideration of the solvent. For each characteristic region, one excitation is referenced. [Color figure can be viewed in the online issue, which is available at wileyonlinelibrary.com.]

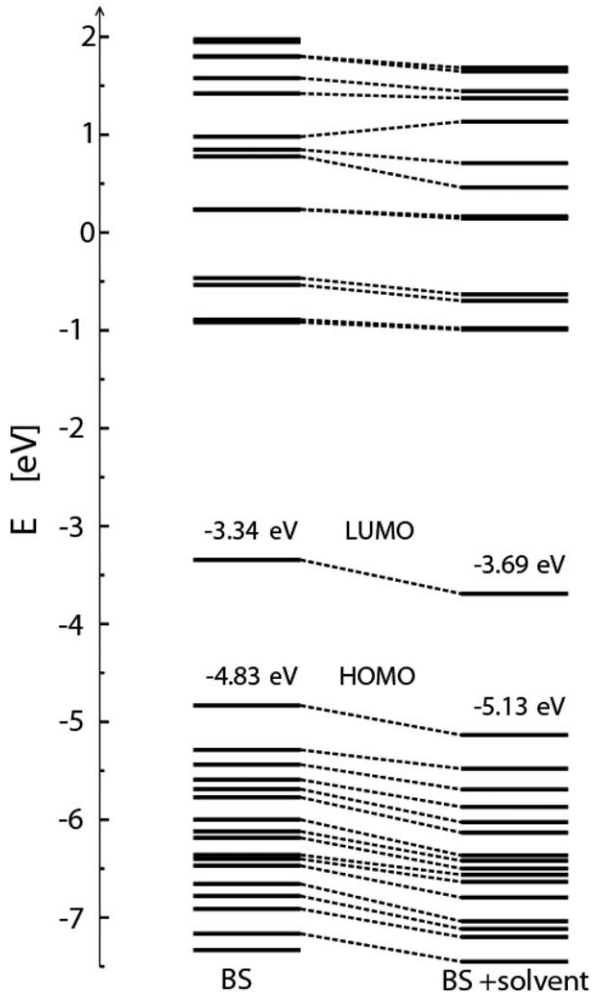


Figure 11. Calculated term scheme with and without the solvent with respect to the vacuum level (0 eV).

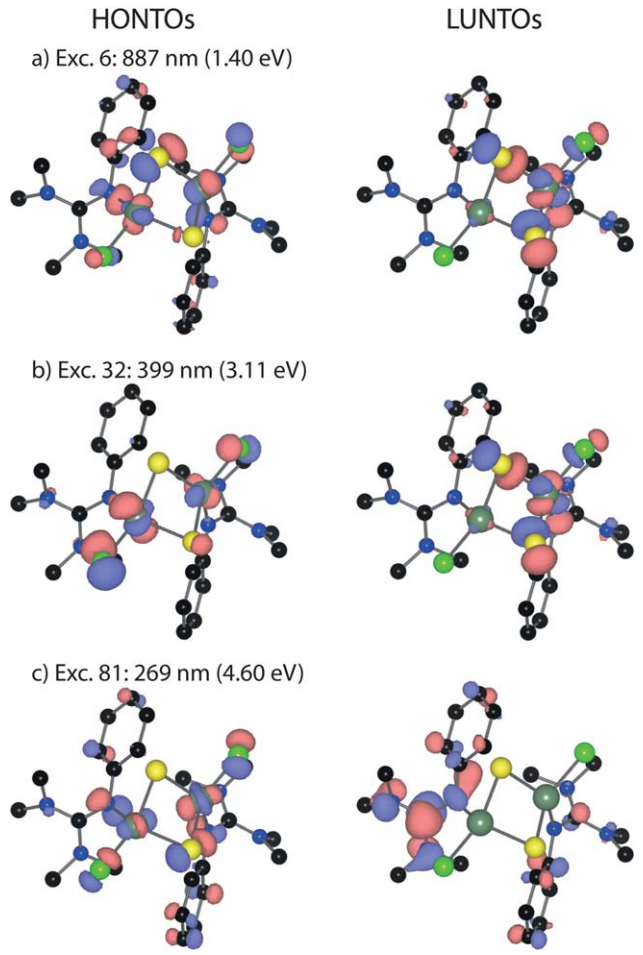


Figure 12. Visualized HONTO and LUNTO pairs for characteristic a) long, b) mid, and c) short wavelength absorption peaks. Only one spin channel is shown here. [Color figure can be viewed in the online issue, which is available at wileyonlinelibrary.com.]

with in the BS method might slightly deviate from the actual geometry.[33,79] Moreover, temperature and solvation effects will also modify slightly the molecular structure. This—in addition to the influence of the functional and the basis set—may affect the accuracy of the calculated molecular vibrations. From calculations using a slightly modified Cu...Cu bond length (± 0.05 Å), we estimate the geometry-related frequency error bar for the diamond-core localized vibrational modes to be of the order of less than 5 $cm^{-1}$.

**Table 3.** Measured and assigned calculated resonance Raman modes according to the data in Figure 14.

| 360-nm excitation | | 720-nm excitation | |
|---|---|---|---|
| Exp | Calc | Exp | Calc |
| 500 | 493 | 124 | 129 |
| 603 | 623 | 174 | 173 |
| 798 | 812 | 199 | 196 |
| 830 | 812 | 258 | 254 |
| 943 | 944 | 283 | 287 |
| 1036 | 1043 | 333 | 340 |
| 1053 | 1057 | 365 | 372 |
| 1090 | 1104 | 398 | 390 |
| 1174 | 1170 | 466 | 465 |
| 1381 | 1366 | 500 | 493 |
| 1598 | 1595 | 538 | 545 |
| | | 620 | 623 |
| | | 737 | 735 |
| | | 816 | 812 |
| | | 880 | 871 |

Units are given in $cm^{-1}$.

The calculations show that Cu-related modes are only observable up to 400 $cm^{-1}$. This corresponds to the strength of Cu-thiolate bonds as already found in blue copper proteins.[23,80] A selection of typical core modes can be found in Figure 13. Due to the puckered geometry of the diamond core, pure in-plane modes do not occur. For most of the core excitations, the Cl ions are displaced as well (compare mode 1, 3, and 4, Fig. 13). To verify our calculations and relate it to the optical properties we present measured resonant Raman data for the two excitation wavelengths 360 and 720 nm, cf. Figure 14. The two wavelengths are chosen to probe the optical excitations at 708 nm and the mid-energy regime around 400 nm which lies right in between the metal-metal and metal to ligand charge transfer regime. The measured modes are assigned to the calculated molecular vibrations following Petrenko et al.[78] As expected, the calculated and measured

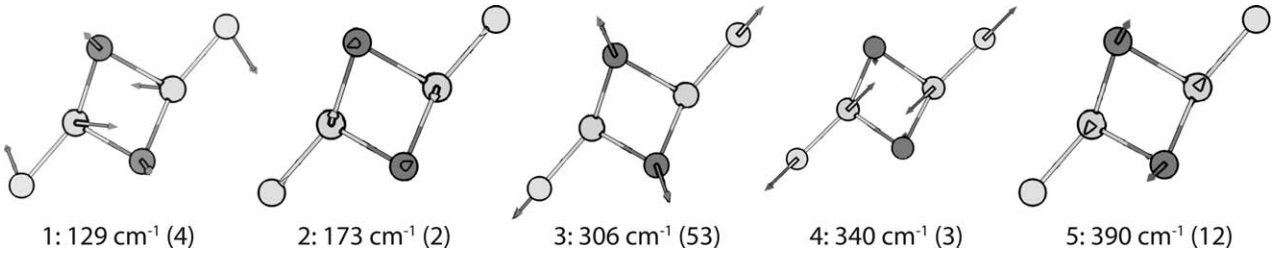


**Figure 13**. Selected Raman active core modes of the complex along with the scaled displacement vectors. In parenthesize are the relative intensities given.

intensities of the Raman shifts do not correspond due to the different absorption cross sections for Raman and resonant Raman intensities.

Although there already exist theoretical calculations incorporating the Franc–Condon–Hertzberg–Teller terms to the Taylor expansion of the transition dipole moment,[81–83] it is not yet a standard procedure in quantum chemical calculations, especially not for large systems containing transition metal elements. With regard to the results in Figure 14, each major experimental peak can be assigned to a theoretical mode. A compilation of the measured and assigned modes is given in Table 3 whereas a detailed picture of each assigned experimental mode can be found in the Supporting Information, Table S6. Unfortunately, the molecular signal between 360 and 500 $cm^{-1}$ is superimposed with the cuvette signal so the enhancement of the Cu-S-Cl modes (which are optically excited around 360 nm) are mostly masked. The measured mode at 304 $cm^{-1}$ is solvent related and does not correspond to the diamond-core mode at 306 $cm^{-1}$ predicted theoretically (see mode 3, Fig. 13).[84]

In the 720 nm spectrum a mode at 398 $cm^{-1}$ appears which can be related to a calculated core deformation mode (Fig. 13, mode 5). In the 360 nm spectrum a hunch around 400 $cm^{-1}$ is visible but due to the cuvette signal one can only speculate that there is the slightly enhanced core deformation mode underneath which is theoretically predicted. The large peak around 700 $cm^{-1}$ is the signal of the solvent as well. For both excitations, there is a visible signal around 800 $cm^{-1}$ although two modes (798 and 830 $cm^{-1}$) are fitted for the 360 nm excitation. On the other side, the calculation shows that only one Raman mode is in this region which lies exactly in between at 812 $cm^{-1}$ being close to the 816 $cm^{-1}$ mode measured at 720 nm. Hence, the two fitted signals seem to be an experimental artifact and only one Raman mode is observed for 360 nm which is a guanidine bending mode.

The high energy shifts above 1000 $cm^{-1}$ have a very high non-resonant intensity. They all belong to Raman modes which are mostly dominated by rocking phenylene modes which can primarily be optically excited with wavelengths less than 300 nm (higher than 4.1 eV). In this long wavelength spectral region only modes involving guanidine are slightly enhanced. So pure phenylene modes are non-resonant for 360 nm. This looks different for the 720-nm excitation where also two low energy shifts can be seen at 538 and 620 $cm^{-1}$.

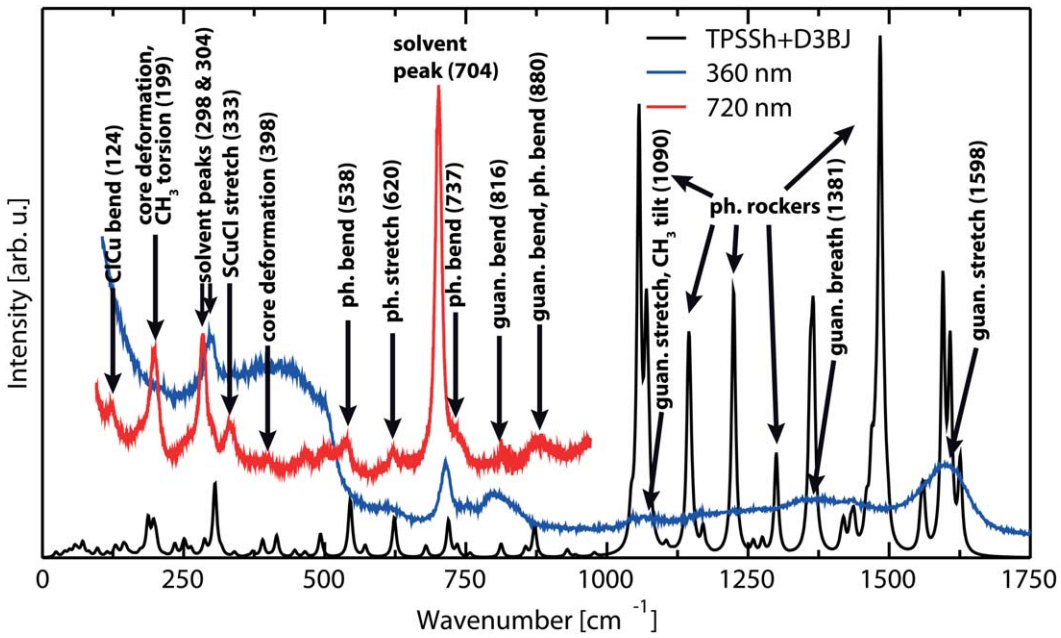


**Figure 14**. Experimental resonant Raman spectrum excited at 360 and 720 nm as well as a calculated non resonant Raman spectrum at the TPSSh + D3BJ/cc-pVDZ equilibrium geometry. The major experimental peaks are labeled according to the assignment to calculated modes, experimental wavenumbers are given in parentheses. [Color figure can be viewed in the online issue, which is available at wileyonlinelibrary.com.]

Also the peak at 880 $cm^{-1}$ is dominantly given by a rocking mode of the phenyls mixing with a stretching of the guanidine. This is reflected in the NTOs given in Figure 10 where one can observe that for low energy transitions a charge transfer to the phenylene rings is noticable. It can be seen that the low energy modes for 720 nm, where sulfur is involved, are more enhanced than the guanidine modes as expected from the optical induced charge transfer toward the S orbitals. Obviously the calculated vibrational properties in conjunction with the calculated optical absorption data are consistent with the resonant Raman data presented above.

## Conclusions

The article complements the analysis of the thiolate bridged HV dinuclear Cu complex studied in Refs. [27,33], where its synthesis and its ground-state geometry and electronic structure were explored. Here, we present a detailed orbital analysis of the electron density and find that the core is strongly covalently bonded by bridging $\sigma$ bonds between the S, Cu and Cl atoms. The *OP* provides that there is no interaction between the two S atoms. A detailed CDA analysis shows that the bonding mechanism is mainly driven between Cu $d_z^2$-orbitals forming $\sigma$ bonds mediated by S-S $\pi$ and $\pi^*$ orbitals. The HOMO and LUMO of the complex are given by symmetry distorted Cu-Cu $d$-$\pi^*$ and $\pi$ orbitals like the MV Tolman complex discussed in Ref. 29 whereas for the here discussed HV complex the interaction is transmitted via the ligands forming a BS complex.

The spectroscopic analysis is straightforward and utilizes TD-DFT calculations combined with an NTO analysis. The influence of the solvent is important to reproduce the experimentally observed data as it revokes certain degenerations, especially at higher lying unoccupied orbitals. The spectrum can be divided into the typical *d-d* transitions for lower energies with the addition of chloride as electron donor and S as acceptor and charge transfer excitations for higher energies above 3.6 eV from the Cu and Cl atoms to the phenyl rings. Concerning the peak positions, the spectrum is comparable to the similar HV complex by Tolman.[29] We present resonant Raman spectra for 360- and 720-nm excitation wavelengths and identify the major peaks by comparison to DFT data. It is found that Cu-S modes are enhanced at both wavelengths, whereas the phenylene modes are only visible in the 360 nm signal. This is consistent with the analysis of the TD-DFT optical absorption data. In conclusion, the present work shows that the $Cu_2$(N-GuaS)$_2Cl_2$ complex is not a $Cu_A$ model in the strict sense, but still provides important insight into the spin structure and charge transfer between copper and the donor atoms in the $Cu_2S_2Cl_2$ core.

## *Acknowledgment*

*Computing time of the Paderborn Center for Parallel Computing ($PC^2$) is gratefully acknowledged.*

**Keywords:** DFT · $Cu_A$ site · TD-DFT · copper thiolate complexes · CDA

How to cite this article: M. Witte, B. Grimm-Lebsanft, A. Goos, S. Binder, M. Rübhausen, M. Bernard, A. Neuba, S. Gorelsky, U. Gerstmann, G., Henkel, W. Gero Schmidt, S. Herres-Pawlis. *J. Comput. Chem.* **2016**, *37*, 2181–2192. DOI: 10.1002/jcc.24439

Additional Supporting Information may be found in the online version of this article.

[1] P. J. Hay, J. C. Thibeault, R. Hoffmann, *J. Am. Chem. Soc.* **1975**, *97*, 4884.
[2] P. Alemany, S. Alvarez, *Inorg. Chem.* **1992**, *31*, 4266.
[3] G. Aullón, G. Ujaque, A. Lledós, S. Alvarez, P. Alemany, *Inorg. Chem.* **1998**, *37*, 804.
[4] A. A. Palacios, G. Aullón, P. Alemany, S. Alvarez, *Inorg. Chem.* **2000**, *39*, 3166.
[5] C. Mealli, A. Ienco, A. Poduska, R. Hoffmann, *Angew. Chem. Int. Ed.* **2008**, *47*, 2864.
[6] S. Iwata, C. Ostermeier, B. Ludwig, H. Michel, *Nature* **1995**, *376*, 660.
[7] M. Wilmanns, P. Lappalainen, M. Kelly, E. Sauer-Eriksson, M. Saraste, *Proc. Natl. Acad. Sci. USA* **1995**, *92*, 11955.
[8] T. Tsukihara, H. Aoyama, E. Yamashita, T. Tomizaki, H. Yamaguchi, K. Shinzawa-Itoh, R. Nakashima, R. Yaono, S. Yoshikawa, *Science* **1995**, *269*, 1069.
[9] G. Henkel, A. Müller, S. Weissgräber, G. Buse, T. Soulimane, G. C. M. Steffens, H. F. Nolting, *Angew. Chem. Int. Ed.* **1995**, *34*, 1488.
[10] N. J. Blackburn, S. De Vries, M. E. Barr, R. P. Houser, W. B. Tolman, D. Sanders, J. A. Fee, *J. Am. Chem. Soc.* **1997**, *119*, 6135.
[11] E. C. Brown, N. W. Aboelella, A. M. Reynolds, G. Aullo, S. Alvarez, W. B. Tolman, *Inorg. Chem. Commun.* **2004**, *43*, 3335.
[12] K. Paraskevopoulos, S. V. Antonyuk, R. G. Sawers, R. R. Eady, S. S. Hasnain, *J. Mol. Biol.* **2006**, *362*, 55.
[13] B. M. Hoffman, J. E. Roberts, M. Swanson, S. H. Speck, E. Margoliash, *Proc. Natl. Acad. Sci. USA* **1980**, *77*, 1452.
[14] T. H. Stevens, C. T. Martin, H. Wang, G. W. Brudvig, C. P. Scholes, S. I. Chan, *J. Biol. Chem.* **1982**, *257*, 12106.
[15] M. Hay, J. H. Richards, Y. Lu, *Proc. Natl. Acad. Sci. USA* **1996**, *93*, 461.
[16] P. Lappalainen, R. Aasa, B. G. Malmström, M. Saraste, *J. Biol. Chem.* **1993**, *268*, 26416.
[17] J. A. Farrar, F. Neese, P. Lappalainen, P. M. H. Kroneck, M. Saraste, W. G. Zumft, A. J. Thomson, D. Karlsruhe, *J. Am. Chem. Soc.* **1996**, *118*, 11501.
[18] C. R. Andrew, R. Fraczkiewicz, R. S. Czernuszewicz, P. Lappalainen, M. Saraste, J. Sanders-Loehr, *J. Am. Chem. Soc.* **1996**, *118*, 10436.
[19] T. Tsukihara, H. Aoyama, E. Yamashita, T. Tomizaki, H. Yamaguchi, K. Shinzawa-Itoh, R. Nakashima, R. Yaono, S. Yoshikawa, *Science* **1996**, *272*, 1136.
[20] P. M. Colman, H. C. Freeman, J. M. Guss, M. Murata, V. A. Norris, J. A. M. Ramshaw, M. P. Venkatappa, *Nature* **1978**, *272*, 319.
[21] K. W. Penfield, A. A. Gewirth, E. I. Solomon, *J. Am. Chem. Soc.* **1985**, *107*, 4519.
[22] S. E. Shadle, J. E. Pennerhahn, H. J. Schugar, B. Hedman, K. O. Hodgson, E. I. Solomon, *J. Am. Chem. Soc.* **1993**, *115*, 767.
[23] D. W. Randall, S. DeBeer George, B. Hedman, K. O. Hodgson, K. Fujisawa, E. I. Solomon, *J. Am. Chem. Soc.* **2000**, *122*, 11620.
[24] E. I. Solomon, R. K. Szilagyi, S. DeBeer George, L. Basumallick, *Chem. Rev.* **2004**, *104*, 419.
[25] E. I. Solomon, B. Hedman, K. O. Hodgson, A. Dey, R. K. Szilagyi, *Coord. Chem. Rev.* **2005**, *249*, 97.
[26] R. P. Houser, V. G. Young, W. B. Tolman, *J. Am. Chem. Soc.* **1996**, *118*, 2101.
[27] A. Neuba, R. Haase, W. Meyer-Klaucke, U. Flörke, G. Henkel, *Angew. Chem. Int. Ed.* **2012**, *51*, 1714.
[28] R. P. Houser, J. A. Halfen, V. G. Young, N. J. Blackbum, W. B. Tolman, *J. Am. Chem. Soc.* **1995**, *117*, 10745.

[29] D. R. Gamelin, D. W. Randall, M. T. Hay, R. P. Houser, T. C. Mulder, G. W. Canters, S. De Vries, W. B. Tolman, Y. Lu, E. I. Solomon, *J. Am. Chem. Soc.* **1998**, *120*, 5246.
[30] E. I. Solomon, X. Xie, A. Dey, *Chem. Soc. Rev.* **2008**, *37*, 623.
[31] M. Gennari, J. Pécaut, S. DeBeer, F. Neese, M. N. Collomb, C. Duboc, *Angew. Chem. Int. Ed.* **2011**, *50*, 5662.
[32] E. C. M. Ording-Wenker, M. van der Plas, M. A. Siegler, S. Bonnet, F. M. Bickelhaupt, C. Fonseca Guerra, E. Bouwman, *Inorg. Chem.* **2014**, *53*, 8494.
[33] M. Witte, U. Gerstmann, A. Neuba, G. Henkel, W. G. Schmidt, *J. Comp. Chem. Phys.* **2016**, *37*, 1005.
[34] C. Trumm, O. Hübner, P. Walter, S. Leingang, U. Wild, E. Kaifer, B. Eberle, H. J. Himmel, *Eur. J. Inorg. Chem.* **2014**, *2014*, 6039.
[35] S. Wiesner, A. Wagner, O. Hübner, E. Kaifer, H. J. Himmel, *Chem. Eur. J.* **2015**, *21*, 16494.
[36] A. Ziesak, T. Wesp, O. Hübner, E. Kaifer, H. Wadepohl, H. J. Himmel, *Dalt. Trans.* **2015**, *44*, 19111.
[37] M. Schatz, V. Raab, S. P. Foxon, G. Brehm, S. Schneider, M. Reiher, M. C. Holthausen, J. Sundermeyer, S. Schindler, *Angew. Chem. Int. Ed.* **2004**, *43*, 4360.
[38] D. Petrovic, L. M. R. Hill, P. G. Jones, W. B. Tolman, M. Tamm, *Dalt. Trans.* **2008**, *2008*, 887.
[39] O. Bienemann, A. Hoffmann, S. Herres-Pawlis, *Rev. Inorg. Chem.* **2011**, *31*, 83.
[40] A. Jesser, M. Rohrmüller, W. G. Schmidt, S. Herres-Pawlis, *J. Comput. Chem.* **2014**, *35*, 1.
[41] A. Hoffmann, M. Rohrmüller, A. Jesser, I. Dos Santos Vieira, W. G. Schmidt, S. Herres-Pawlis, *J. Comput. Chem.* **2014**, *2014*, 2146.
[42] S. I. Gorelsky, X. Xie, Y. Chen, J. A. Fee, E. I. Solomon, *J. Am. Chem. Soc.* **2006**, *128*, 16452.
[43] L. Noodleman, J. G. Norman, *J. Phys. Chem.* **1979**, *70*, 4903.
[44] L. Noodleman, *J. Chem. Phys.* **1981**, *74*, 5737.
[45] L. Noodleman, E. J. Baerends, *J. Am. Chem. Soc.* **1984**, *106*, 2316.
[46] L. Noodleman, D. Case, *Adv. Inorg. Chem.* **1992**, *38*, 423.
[47] F. Neese, *Coord. Chem. Rev.* **2009**, *253*, 526.
[48] E. Ruiz, M. Llunell, P. Alemany, *J. Solid State Chem.* **2003**, *176*, 400.
[49] C. J. Calzado, J. Cabrero, J. P. Malrieu, R. Caballol, *J. Chem. Phys.* **2002**, *116*, 3985.
[50] M. Zbiri, S. Saha, C. Adhikary, S. Chaudhuri, C. Daul, S. Koner, *Inorg. Chim. Acta* **2006**, *359*, 1193.
[51] A. Hoffmann, S. Herres-Pawlis, *Chem. Commun.* **2014**, *50*, 403.
[52] A. Hoffmann, S. Herres-Pawlis, *Phys. Chem. Chem. Phys.* **2016**, *18*, 6430.
[53] J. Tao, J. Perdew, V. Staroverov, G. Scuseria, *Phys. Rev. Lett.* **2003**, *91*, 146401.
[54] V. N. Staroverov, G. E. Scuseria, J. Tao, J. P. Perdew, *J. Chem. Phys.* **2003**, *119*, 12129.
[55] V. N. Staroverov, G. E. Scuseria, J. Tao, J. P. Perdew, *J. Chem. Phys.* **2004**, *121*, 11507.
[56] M. J. Frisch, G. W. Trucks, H. B. Schlegel, G. E. Scuseria, M. A. Robb, J. R. Cheeseman, G. Scalmani, V. Barone, B. Mennucci, G. A. Petersson, H. Nakatsuji, M. Caricatos, X. Li, H. P. Hratchian, A. F. Izmaylov, J. Blooine, G. Zheng, J. L. Sonnenberg, M. Hada, M. Ehara, K. Toyota, R. Fukuda, J. Hasegawa, M. Ishida, T. Nakajima, Y. Honda, O. Kitao, H. Nakai, T. Vreven, J. A. Montgomery Jr., J. E. Peralta, F. Ogliaro, M. Bearpark, J. J. Heyd, E. Brothers, K. N. Kudin, V. N. Staroverov, R. Kobayashi, J. Normand, K. Raghavachari, A. Rendell, J. C. Burant, S. S. Iyengar, J. Tomasi, M. Cossi, N. Rega, J. M. Millam, M. Klene, J. E. Knox, J. B. Cross, V. Bakken, C. Adamo, J. Jaramillo, R. Gomperts, R. E. Stratmann, O. Yazyev, A. J. Austin, R. Cammi, C. Pomelli, J. W. Ochterski, R. L. Martin, K. Morokuma, V. G. Zakrzewski, G. A. Voth, P. Salvador, J. J. Dannenberg, S. Dapprich, A. D. Daniels, Ö. Farkas, J. B. Foresman, J. V. Ortiz, J. Cioslowski, D. J. Fox, Gaussian09, Revision D01; **2009**. Gaussian Inc. Wallinford, CT.
[57] S. Grimme, *J. Comput. Chem.* **2006**, *27*, 1787.
[58] S. Grimme, S. Ehrlich, L. Goerigk, *J. Comput. Chem.* **2011**, *32*, 1456.
[59] T. H. Dunning, Jr., *J. Chem. Phys.* **1989**, *90*, 1007.
[60] N. B. Balabanov, K. A. Peterson, *J. Chem. Phys.* **2005**, *123*, 064107.
[61] D. E. Woon, T. H. Dunning, Jr., *J. Chem. Phys.* **1993**, *98*, 1358.
[62] M. E. Casida, *J. Mol. Struct. THEOCHEM* **2009**, *914*, 3.
[63] S. I. Gorelsky, AOMix: Program for Molecular Orbital Analysis, version 6.87, **2015**. Available at: http://www.sg-Chem.net/.
[64] B. Schulz, J. Bäckström, D. Budelmann, R. Maeser, M. Rübhausen, M. V. Klein, E. Schoeffel, A. Mihill, S. Yoon, *Rev. Sci. Instrum.* **2005**, *76*, 073107.
[65] I. Haslingerova, *Czech. J. Phys.* **1977**, *B27*, 1389.
[66] M. D. Segall, R. Shah, C. J. Pickard, M. C. Payne, *Phys. Rev. B* **1996**, *54*, 16317.
[67] W. V. Glassey, R. Hoffmann, *J. Chem. Phys.* **2000**, *113*, 1698.
[68] S. Alvarez, R. Hoffmann, C. Mealli, *Chem. Eur. J.* **2009**, *15*, 8358.
[69] R. Ponec, E. Ramos-Cordoba, P. Salvador, *J. Phys. Chem. A* **2013**, *117*, 1975.
[70] F. Neese, W. G. Zumft, W. E. Antholine, P. M. H. Kroneck, *J. Am. Chem. Soc.* **1996**, *118*, 8692.
[71] Y. Takano, Y. Shigeta, K. Koizumi, H. Nakamura, *Int. J. Quantum Chem.* **2012**, *112*, 208.
[72] R. Gurbiel, Y. Fann, K. K. Surerus, M. M. Werst, S. M. Musser, P. E. Doan, S. I. Chan, J. A. Fee, B. M. Hoffman, *J. Am. Chem. Soc.* **1993**, *115*, 10888.
[73] S. DeBeer George, M. Metz, R. K. Szilagyi, H. Wang, S. P. Cramer, Y. Lu, W. B. Tolman, B. Hedman, K. O. Hodgson, E. I. Solomon, *J. Am. Chem. Soc.* **2001**, *123*, 5757.
[74] S. Miertus, E. Scrocco, J. Tomasi, *Chem. Phys. 55*, 117 (**1981**).
[75] M. Cossi, V. Barone, R. Cammi, J. Tomasi, *Chem. Phys. Lett.* **1996**, *255*, 327.
[76] M. Cossi, G. Scalmani, N. Rega, V. Barone, *J. Chem. Phys.* **2002**, *117*, 43.
[77] R. L. Martin, *J. Chem. Phys.* **2003**, *118*, 4775.
[78] T. Petrenko, K. Ray, K. E. Wieghardt, F. Neese, *J. Am. Chem. Soc.* **2006**, *128*, 4422.
[79] J. P. Malrieu, G. Trinquier, *J. Phys. Chem. A* **2012**, *116*, 8226.
[80] E. I. Solomon, S. I. Gorelsky, A. Dey, *J. Comput. Chem.* **2006**, *27*, 1415.
[81] M. Dierksen, S. Grimme, *J. Chem. Phys.* **2004**, *120*, 3544.
[82] M. Dierksen, S. Grimme, *J. Phys. Chem. A* **2004**, *108*, 10225.
[83] A. Baiardi, J. Bloino, V. Barone, *J. Chem. Phys.* **2014**, *141*, 114108.
[84] A. Hoffmann, S. Binder, A. Jesser, R. Haase, U. Flörke, M. Gnida, M. Salomone Stagni, W. Meyer-Klaucke, B. Lebsanft, L. E. Grünig, S. Schneider, M. Hashemi, A. Goos, A. Wetzel, M. Rübhausen, S. Herres-Pawlis, *Angew. Chem. Int. Ed.* **2014**, *53*, 299.

Received: 3 March 2016
Revised: 10 June 2016
Accepted: 13 June 2016
Published online on 30 June 2016